Journal of Electronic Materials (2024) 53:5062–5072
https://doi.org/10.1007/s11664-024-11139-0

28TH INTERNATIONAL CONFERENCE ON NUCLEAR TRACKS AND RADIATION MEASUREMENTS

Modification of the Electrical Properties of a $Bi_{0.8}Ca_{0.2}FeO_3/LaNiO_3/LaAlO_3$ Heterostructure: Effect of 80 MeV O^{+7} Ion Irradiation

Sumana Hajra[1] · P. Josely Jose[1,2] · Urjitsinh I. Rathod[1] · Mukesh Keshvani[2,3] · Jayaprakash Sahoo[4] · Megha Vagadia[4,5] · R. Meena[6] · S. Ojha[6] · Ashish Ravalia[1]

Received: 15 December 2023 / Accepted: 22 April 2024 / Published online: 18 May 2024

Abstract

Ca-doped $BiFeO_3/LaNiO_3/LaAlO_3$ (BCFO/LNO/LAO) heterostructures have garnered significant interest due to their unique combination of ferroelectric, magnetic, and resistive switching properties due to interfaces and lattice mismatch/strain, leading to unique electronic properties. The roles of structural defects and oxygen vacancies are important in achieving the magnetic and electrical properties of $BiFeO_3$-based heterostructures. By generating defects, swift heavy ion irradiation can lead to changes in the structural, optical, electrical, and magnetic properties of the materials. The Ca-doped $BiFeO_3$ and $LaNiO_3$ heterostructure was grown upon LAO substrates using the pulsed laser deposition technique, ensuring high-quality interfaces and controlled thicknesses. The heterostructures were irradiated with 80 MeV O^{+7} ions at various ion fluence levels (5×10^{10} ions/cm^2 to 5×10^{12} ions/cm^2). The structure and crystalline orientation of the thin films were confirmed through x-ray diffraction, while the surface morphology was measured using atomic force microscopy. Irradiation-induced modifications of the structural strain and surface morphology were investigated in the context of internal annealing effect and defect formation. The resistive switching (RS) properties of the proposed devices were assessed by I–V measurement with sweeping $0\rightarrow5\ V\rightarrow0\rightarrow-5\ V\rightarrow0$, which shows that irradiation-induced defects play an important role in the electrical properties of the proposed heterostructure. Bipolar RS behavior was also verified with the conduction mechanism, indicating that the ohmic and space-charge-limited conduction mechanism plays an important role in irradiated BCFO/LNO/LAO heterostructures.

✉ Ashish Ravalia
ashishravalia@gmail.com

[1] Department of Nanoscience and Advanced Materials, Saurashtra University, Rajkot 360005, India

[2] Department of Physics, Marwadi University, Rajkot 360003, India

[3] The Patidar Gin Science College, Bardoli 394601, India

[4] Department of Physics, Indian Institute of Science Education and Research, Bhopal 462066, India

[5] Department of Physics, Saurashtra University, Rajkot 360005, India

[6] Inter-University Accelerator Centre, Aruna Asaf Ali Marg, New Delhi 110067, India

Graphical Abstract

Graphical representation of the defect formation and RS behavior due to varying ion fluence as a function of RMS roughness and strain.

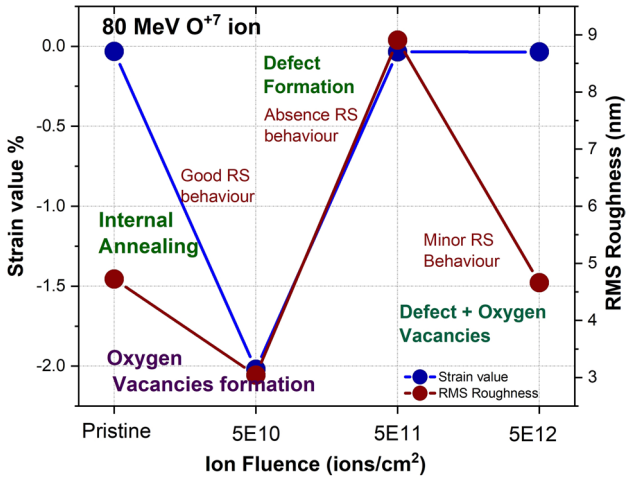

Keywords Thin-film heterostructures · SHI irradiation · defects · BFO · resistive switching

Introduction

Advancements in materials science and nanotechnology have paved the way for the exploration of novel functional materials and their potential applications in electronic devices.[1] One such intriguing class of materials is multiferroic heterostructures, which exhibit a unique combination of ferroelectric and ferromagnetic properties, making them promising candidates for a wide range of applications, including nonvolatile memory devices, spintronic devices, and beyond.[2] The intricate interplay of different layers within these heterostructures, along with their tunable properties, holds the key to unlocking their full potential.[3]

$BiFeO_3$ (BFO) is a multiferroic compound known for exhibiting the coexistence of ferroelectric and antiferromagnetic ordering above room temperature.[4–6] When incorporated into heterostructures with other materials, BFO can exhibit a wide range of intriguing and tunable properties.[7] BFO-based heterostructures have been studied in many dimensions of materials research, including multiferroicity and magnetoelectric coupling, ferroelectric tunnel junctions, piezoelectric and ferroelectric properties, spintronics devices, optoelectronic applications, topological insulators and quantum phenomena, growth techniques and interface engineering, ion irradiation and strain effects, environmental and biomedical applications, and photovoltaic applications.[8–12]

BFO, as a ferroelectric material, exhibits interesting ferroelectric and multiferroic behavior in BFO/LNO heterostructures. The interplay between the ferroelectric polarization of BFO and metallic-magnetic properties of LNO has been a subject of intense study.[13–15] Researchers have explored the impact of strain, thickness, and epitaxial growth conditions on the properties of BFO/LNO heterostructures. These factors can tune the electronic, magnetic, and ferroelectric properties at the interface.[13] Understanding the charge transfer mechanisms and band alignment at the BFO/LNO interface is crucial for designing functional electronic devices. Studies have focused on characterizing the electronic structure and charge distribution at this interface.[16] The magnetoelectric coupling in BFO/LNO heterostructures is of particular interest due to the coexistence of ferroelectric and magnetic order. This coupling has implications for novel spintronic and memory device applications.[17] The interface between BFO and LNO can host a two-dimensional electron gas (2DEG) with intriguing properties. Researchers have investigated the formation and control of this 2DEG for potential applications in electronic devices.[18] BFO/LNO heterostructures have shown promise in photovoltaic and photocatalytic applications, with the potential for efficient solar energy conversion and environmental remediation.[19] The resistive switching behavior of BFO/LNO heterostructures has led to their exploration for nonvolatile memory applications. The resistive switching phenomenon in these heterostructures refers to the ability to reversibly change the electrical resistance of the device between two states, typically a high-resistance state (HRS) and a low-resistance state (LRS), by the application of an external voltage. This behavior is crucial for the development of resistive random-access memory (RRAM) devices.[20] Researchers have employed various

deposition techniques, such as pulsed laser deposition and molecular beam epitaxy, to grow high-quality BFO/LNO heterostructures with well-defined properties. The growth methods are crucial for achieving the desired functionalities.[16] BFO/LNO heterostructures have been extended to superlattice configurations, where alternating layers of BFO and LNO are used to create unique structures with tailored properties.[21]

Electronic excitation induced by swift heavy ions plays an important role in modifying the properties of multiferroic thin films.[22–25] When an energetic ion passes through the material, it loses its energy, which can be converted into the formation of defects (vacancies, interstitials, and dislocations), structural and surface modifications, ion track formation, thermal effects (local heating), the formation of oxygen vacancies (OVs), and modifications in magnetic, electrical, and optical properties.[26,27] Controlled irradiation can be used to engineer the bandgap and magnetic anisotropy for tailoring the properties of oxide heterostructures for specific applications. Ion irradiation is also useful for engineering the interface of thin-film heterostructures under different irradiation effects for modification of the physical properties.

In the present case, we have chosen the 20% Ca-doped $BiFeO_3$ system as the top layer of the heterostructure due to the naturally occurring OVs that function as donor impurities to compensate calcium acceptors and retain a highly stable Fe^{3+} valence state. The reason for choosing $LaNiO_3$ as a second layer is its (i) conducting nature, acting as bottom electrode, and (ii) good lattice mismatch with $LaAlO_3$ substrate. In addition, the effect of swift heavy ion irradiation on the conductivity has been already studied.[28–31]

In this study, we have fabricated oxide multiferroic-based heterostructures by investigating the electrical properties of $Bi_{0.8}Ca_{0.2}FeO_3/LaNiO_3/LaAlO_3$ and exploring the intriguing effects of high-energy ion irradiation. By subjecting this heterostructure to 80 MeV O^{+7} ion irradiation, we aim to shed light on the fundamental changes that occur in the resistive switching properties of this material and gain a deeper understanding of interface engineering with the role of OVs and structural defects and their underlying mechanisms. In addition, understanding the effects of different ion fluence irradiation on the electrical properties of multiferroic heterostructures not only is of fundamental scientific interest but also holds significant promise for the development of next-generation electronic and spintronic devices.

Experimental Techniques

In the present study, $Bi_{0.8}Ca_{0.2}FeO_3/LaNiO_3/LaAlO_3$ thin-film heterostructures were fabricated using pulsed laser deposition (PLD). Figure 1 shows a schematic view of the proposed heterostructure. The polycrystalline bulk targets

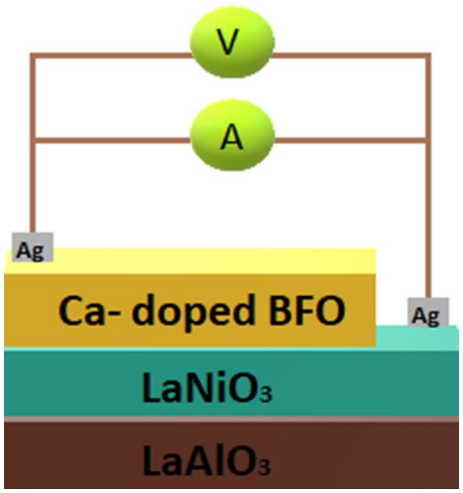

Fig. 1 Schematic of the geometry of the BCFO/LNO/LAO heterostructure.

of $Bi_{0.8}Ca_{0.2}FeO_3$ (BCFO) and $LaNiO_3$ (LNO) were synthesized using the conventional solid-state reaction (SSR) method. The first layer of LNO was grown as a buffer layer on the LAO substrate using a 248 nm KrF excimer laser with 255 mJ energy, 5 Hz repetition rate, and distance between the target and substrate of 5 cm. The substrate temperature and oxygen partial pressure were kept at 550°C and 0.01 kPa, respectively, during the deposition, and all films were deposited for 15 min. The second layer of BCFO was grown on the LNO layer using a 248 nm KrF excimer laser with 240 mJ energy, 5 Hz repetition rate, and distance between the target and substrate of 5 cm. The substrate temperature and oxygen partial pressure were kept at 650°C and 0.01 kPa, respectively, during the deposition, and all films were deposited for 60 min. The substrate was first cut into four pieces of 5 mm × 5 mm for deposition of the LNO and BCFO layer in a single deposition to maintain the same conditions.

These films were then irradiated by 80 MeV O^{+7} ions with fluence values of 5×10^{10} (5E10), 5×10^{11} (5E11), and 5×10^{12} (5E12) ions/cm^2 at IUAC, New Delhi, using a 15 UD tandem accelerator. The estimated current and vacuum were 0.7 pnA and 5×10^{-6} mbar, respectively. The ion beam was focused onto a spot of ~1 mm diameter and was continuously scanned over the complete area of the film using a magnetic scanner to ensure uniform irradiation. To avoid the channeling effect, the irradiation experiments were performed at a normal angle with respect to the ion beam direction. Electron energy loss (Se) and nuclear energy loss (Sn) (using SRIM-2008 software[32]) were calculated using SRIM simulation, and the values were ~0.92 keV/nm and 0.52 eV/nm, respectively. The projectile range of O ions was ~64.47 µm, confirming that the energetic ion passes through the heterostructure.

X-ray diffraction (XRD) measurements of the pristine and irradiated heterostructures were carried out at room temperature using a Bruker D8 x-ray diffractometer with Cu-K_α radiation diffraction. Atomic force microscopy (AFM) measurements were carried out to analyze the surface modifications after irradiation using an NTEGRA Prima atomic force microscope. Cyclic current–voltage (I–V) measurements were carried out by sweeping bias from −5 V to 0 V to +5 V in the geometry given in Fig. 1 using a Keithley 2612A SourceMeter. The Rutherford backscattering (RBS) experiment was conducted using a 3.037 MeV He^+ ion beam at IUAC, New Delhi, to understand the thickness, composition, and interface of the proposed heterostructures.

Results and Discussion

The XRD patterns of pristine and 80 MeV O^{7+} ion-irradiated BCFO/LNO/LAO thin-film heterostructures are shown in Fig. 2. It can be seen that all pristine and irradiated heterostructures show the (h00)-oriented growth of BCFO and LNO along the LAO (h00) substrate orientation. In addition, a minor phase of a (110)-oriented peak of BCFO is also observed, which is compared with the polycrystalline bulk data of BCFO. It is also verified that the commonly observed impurity peak of Bi_2O_3 and $Bi_2Fe_4O_9$ in BFO multiferroics is not present in the present case. The lattice mismatch between the BCFO layer and LAO substrate can be clearly seen from the separation of the film and the substrate XRD peaks, resulting in the strain δ. The values of lattice mismatch or strain in the films at the interface were calculated using the formula

$$\delta\,\% = \left(d_{\text{sub}} - d_{\text{film}}\right)/d_{\text{sub}} * 100\% \tag{1}$$

where d is the d-spacing of the substrate and thin film. The structural strain starts to decreases after 5E10 fluence irradiation and then starts to increase with ion fluence of 5E11 and 5E12, as can be observed in the enlarged view (right panel) of the main peak in Fig. 2. The calculated strain values of BCFO and LAO for the pristine and irradiated heterostructures are tabulated in Table I, and show negative values, suggesting the presence of compressive strain. In addition, there is no variation in the LNO peak observed after irradiation. It is well known that swift heavy ion irradiation can create structural defects, local annealing, or both due to electron energy loss, which is highly dependent on the ion fluence.[33,34] In the present case, the large decrease in strain in the 5E10-irradiated heterostructure suggests that the internal annealing effect becomes more prominent, while the minor variation in the strain of the 5E11- and 5E12-irradiated heterostructures is due to the formation of structural defects and hence an increase in unit cell volume.

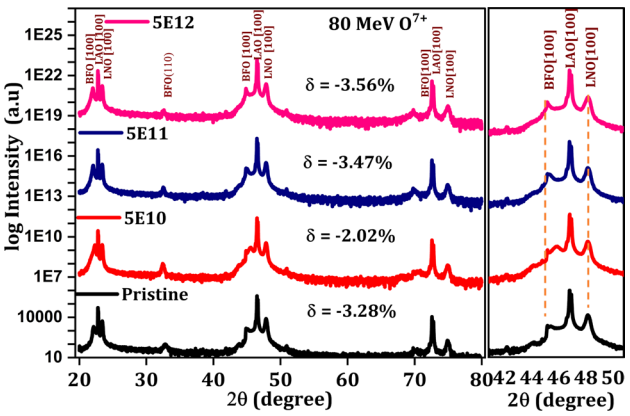

Fig. 2 XRD diffraction patterns of pristine and irradiated BCFO/LNO/LAO heterostructures.

Figure 3a, b, c, and d show the AFM micrograph of 2D and 3D images, height distribution, surface profiles of pristine, and the irradiated top surface of the BCFO/LNO/LAO heterostructures. It can be seen from Fig. 3a and b that the pristine heterostructure surface shows a partially developed granular structure, while after 5E10 fluence irradiation, it shows a fully granular structure, and with further irradiation at 5E11 and 5E12, a linear track-like feature and near-track feature with hillocks, respectively, are observed. The linear track-like feature and near-track with hillocks are the signature of the displacement and rearrangements within the crystal lattice caused by the energy and momentum transferred from the incident ions to the target atoms, which modifies the structure and local electronic structure.[35] Figure 3c depicts the topographical images, which show the homogeneous distribution event for 5E10 irradiation compared with the pristine heterostructure and higher-fluence irradiation (5E11 and 5E12) images, which show a random distribution. The average root mean square (RMS) surface roughness, average height, and maximum height are tabulated in Table I, in which all the values increase for the 5E11-irradiated heterostructure, indicating the formation of surface defects due to irradiation, and decrease in the 5E10-irradiated heterostructure, suggesting local annealing due to irradiation. This defect-induced change in 5E11 and 5E12 is observed in the surface profile images (Fig. 3d).

Table I Values of Structural strain, RMS roughness, and average and maximum height for pristine and irradiated BCFO/LNO/LAO heterostructures

Sample name	RMS roughness (nm)	Average height (nm)	Maximum height (nm)	Strain value (%)
Pristine	4.72	9.55	24.82	−3.28
5E10	3.04	9.77	20.39	−2.02
5E11	8.91	22.78	42.89	−3.47
5E12	4.65	9.96	23.10	−3.56

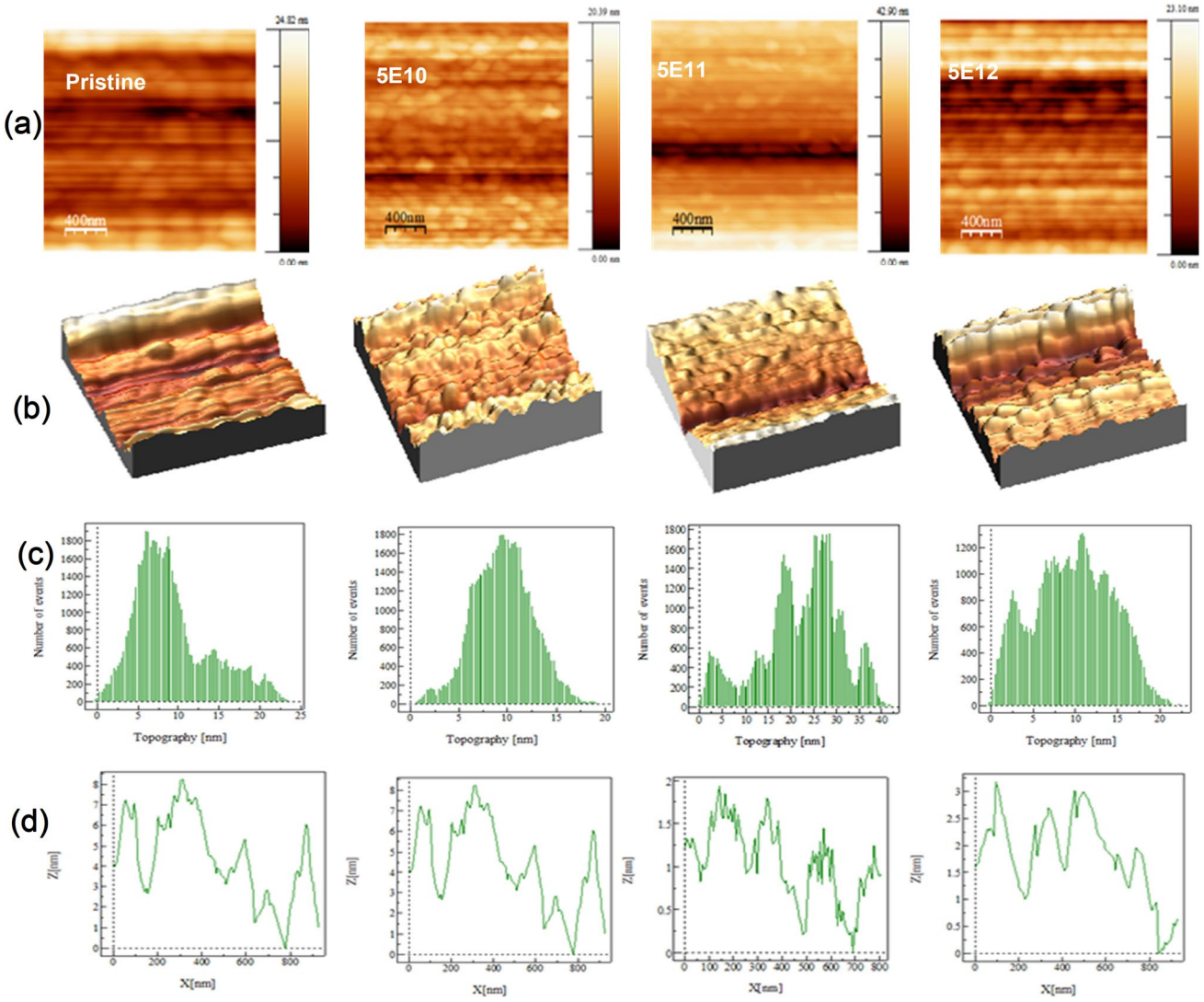

Fig. 3 AFM (a) 2D images, (b) 3D images, (c) topography, and (d) surface profiles of pristine and irradiated BCFO/LNO/LAO heterostructures.

In addition, the separation distance between two grains increases for 5E11 irradiation, which can be understood by the agglomeration of grains due to the higher fluence and formation of defects, and hence noise in curvature, while the 5E12-irradiated sample shows a large change in the surface profile curve due to agglomeration.

Figure 4a, b, c, and d show the raw and RUMP (Rutherford Universal Manipulation Program)-simulated RBS spectra of pristine and 5E10- and 5E11-irradiated BCFO/LNO/LAO heterostructures. RBS data were measured using a 3.037 MeV He^+ ion beam. It can be seen from Fig. 4a that all the elements of the heterostructure are present. The pristine heterostructure shows sharp peaks of Bi and La, indicating homogeneous grain growth, which is modified after 5E10 and 5E11 irradiation. The calculated thicknesses of BCFO and layers in all heterostructures are ~250 nm and ~145 nm, respectively. The simulated graphs of the 5E10- and 5E11-irradiated heterostructures show the mixed phase of BCFO/LNO(encircled in Fig. 4a), which indicates the greater mixed-phase variation with 5E10 irradiation as compared with the pristine and 5E11-fluence irradiation.

To investigate the RS properties of the pristine and irradiated BCFO/LNO/LAO heterostructures, the cyclic I–V behavior was determined in current-perpendicular mode (Fig. 1) geometry. Figure 5a, b, c, and d show the cyclic I–V behavior of the pristine and irradiated heterostructures under the sweeping maximum voltages of $0 \rightarrow 5\ V^{(cycle\ 1)} \rightarrow 0^{(cycle\ 2)} \rightarrow -5\ V^{(cycle\ 3)} \rightarrow 0^{(cycle\ 4)}$ at 100 K, 300 K, and 350 K. All heterostructures show linear behavior with hysteresis in the current value or RS behavior under applied voltage in some of the irradiated heterostructures.

It can be seen from Fig. 5a that the pristine heterostructure does not show any RS behavior at 300 K and 350 K, while it shows minor RS behavior in the higher-voltage ±5 V

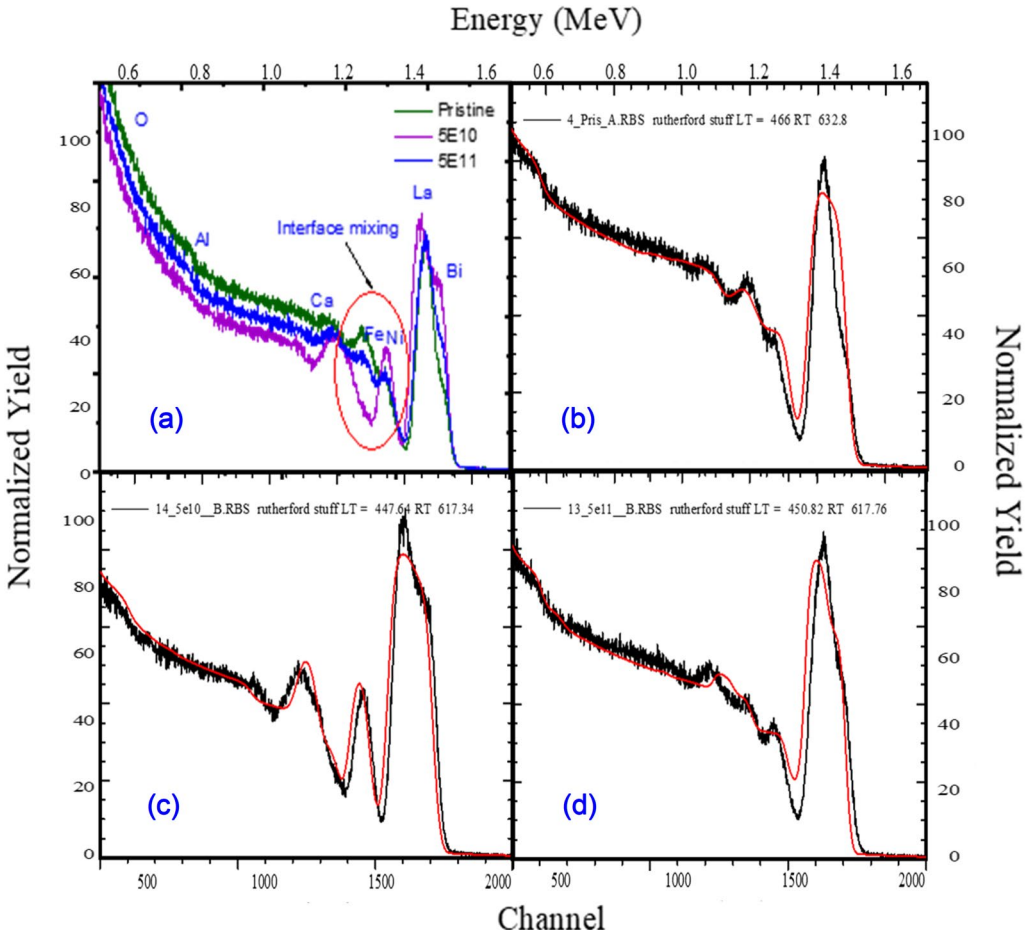

Fig. 4 (a) RBS raw data and RUMP simulated data for (b) pristine and (c) 5E10- and (d) 5E11-fluence irradiated BCFO/LNO/LAO heterostructures.

cycle at 100 K. This behavior of the pristine heterostructure is modified after irradiation. After 5E10 ion irradiation (Fig. 5b), a similar change is observed in the current in positive voltage and negative voltage sweeping cycles at 300 K and 350 K, indicating bipolar RS, whereas at 100 K, large RS behavior is observed, but it is not similar in the positive and negative sides. With further increases in ion irradiation fluence of 5E11 (Fig. 5c), the RS is not significant at 300 K and 350 K, but in the case of 100 K, minor RS behavior is observed. At very high fluence of 5E12 irradiation [Fig. 5d], the RS behavior is significant at 300 K, while at 350 K, it decreases, and for 100 K, no RS behavior is observed.

The RS in BCFO/LNO/LAO heterostructures may be attributed to various mechanisms, including the migration of OVs, the modulation of the interface between different layers, and the changes in the electronic and magnetic properties of the materials involved.[36] In the present case, the formation of OVs and structural defects and interface modification of the BCFO/LNO layer is due to 80 MeV O^{+7} ion irradiation. The modification in temperature-dependent RS behavior of BCFO/LNO/LAO heterostructures as a function of ion fluence is summarized as follows:

(1) In the pristine heterostructure, OVs are formed to maintain the charge neutrality and ionization OVs in the Ca-doped BFO layer. These OVs are distributed in the ferroelectric layer and play an important role in charge conduction and RS behavior due to migration of OVs and the interface effect.[36] In the present case, charge conduction is observed due to formation of OVs. There is an absence of RS behavior due to the bottom LNO conducting layer at 300 K. At 350 K the additional temperature effect enhances the conduction only, and absence of RS behavior is observed. At low temperature (100 K), OVs cannot release the electron in the conduction path up to ±4 V, while at ±5 V it starts to release and create a conduction path in cycle 1, and hence in cycle 2 it shows a low-resistance state with minor RS behavior.

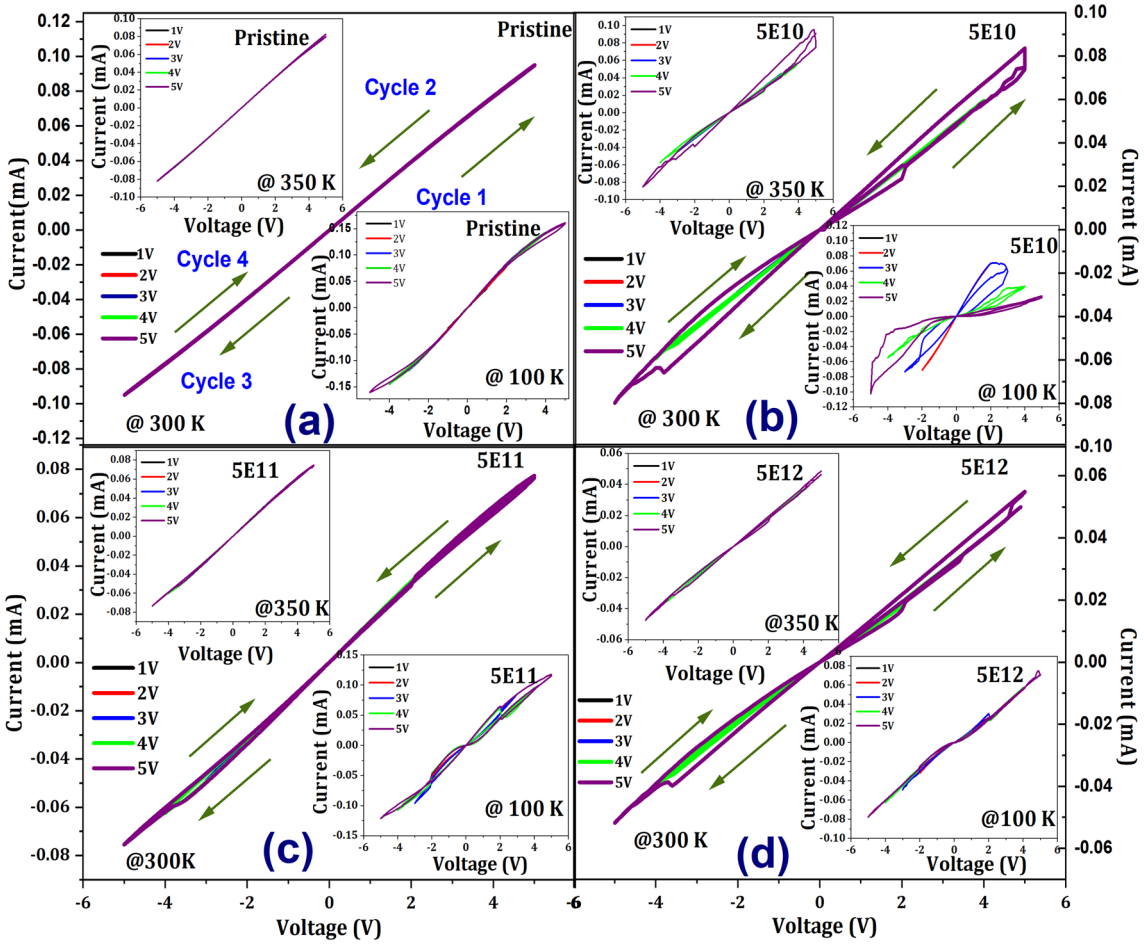

Fig. 5 Cyclic I–V data taken at 100 K, 300 K, and 350 K for (a) pristine and (b) 5E10-, (c) 5E11-, and (d) 5E12-fluence irradiated BCFO/LNO/LAO heterostructures.

(2) The heterostructure irradiated with 5E10 ion fluence shows a reduction in structural strain (confirmed by XRD) and a decrease in roughness and granular structure in AFM images, indicating that local annealing takes place during the 5E10 ion fluence irradiation which forms OVs. In this case, BCFO/LNO interface modification and formation of OVs play an important role in RS behavior at 300 K. RS behavior at 350 K decreases due to the increasing temperature, which facilitates the release of electrons from OVs in cycle 1, and in cycle 2, there are fewer remaining electrons, hence reducing RS behavior. At low temperature (100 K), the enhancement in RS behavior with the asymmetric I–V in positive and negative bias regions may be due to the release of defect-mediated trapped charges at the bottom of the BCFO/LNO under an applied electric field. Similar behavior is observed in PZT/SNTO and BFO films.[37] The temperature-dependent I–V study of the 5E10 heterostructure confirms that interface-assisted detrapping of interfacial charge carrier may responsible for the enhancement in RS behavior, which can be correlated with the modification of the interface in RBS analysis.

(3) The 5E11 ion-irradiated heterostructure does not show RS behavior due to formation of structural defects, which hinders the path of charge carriers released from OVs. Applying a ±5 V sweeping cycle at 300 K, it shows minor RS behavior due to migration of trapped charge carriers at higher voltage. The formation of structural defects can be correlated with the increased structural surface strain and linear track-like surface modification, as observed in XRD and AFM measurements. It is also correlated with the interface modification in RBS analysis.

(4) The 5E12-irradiated heterostructure shows low RS behavior compared with the 5E10-irradiated heterostructure. In this case, the higher-fluence 5E12 irradiation leads to the formation of large structural defects as well as OVs, which both affect the RS behavior. Importantly, an increase in the structural strain and

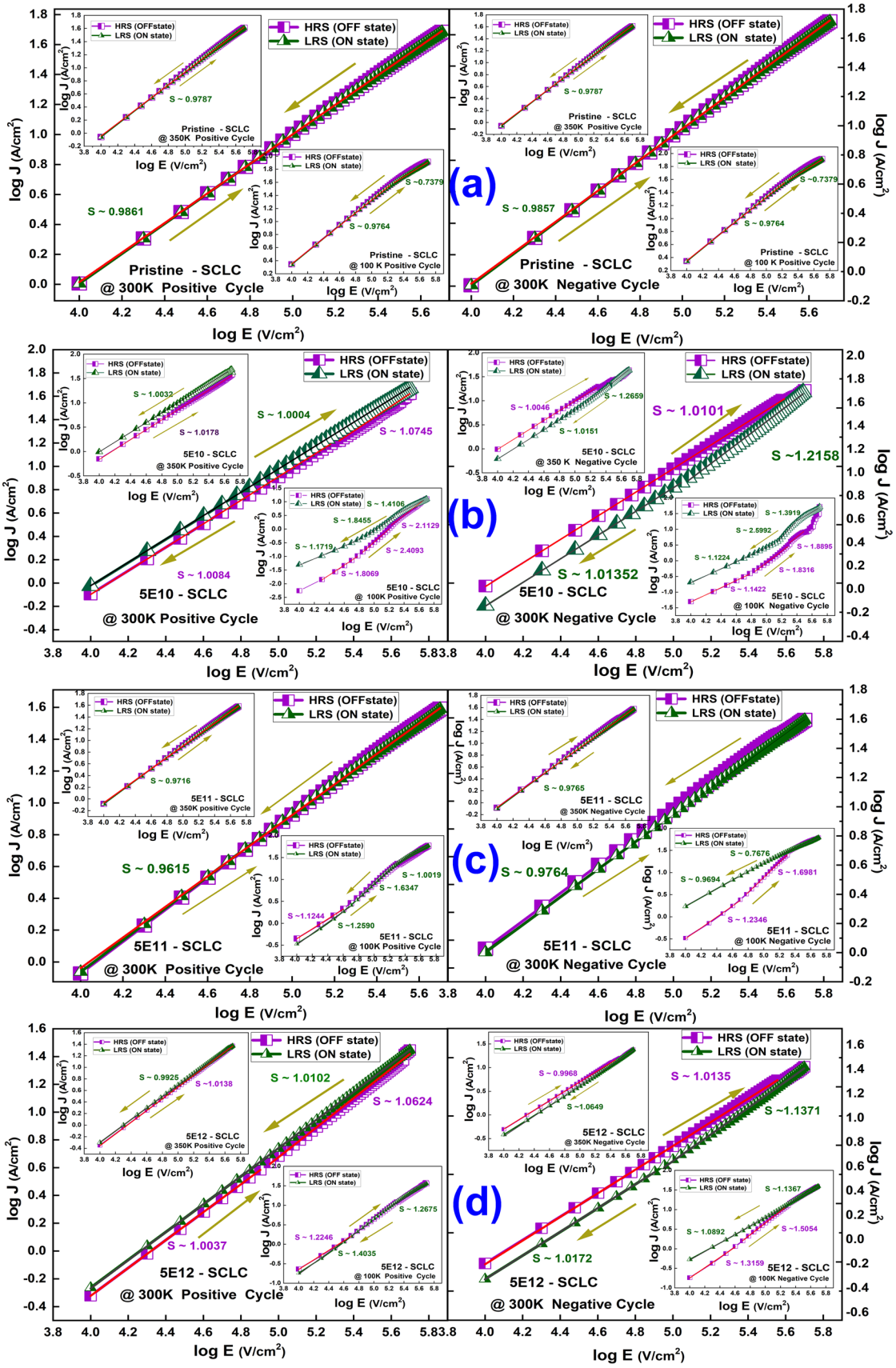
(a)
HRS (OFF state)
LRS (ON state)
S ~ 0.9787
Pristine - SCLC
@ 350K Positive Cycle
S ~ 0.9861
Pristine - SCLC
@ 300K Positive Cycle
S ~ 0.9857
Pristine - SCLC
@ 300K Negative Cycle
S ~ 0.9764
Pristine - SCLC
@ 100 K Positive Cycle
S ~-0.7379
(b)
S ~ 1.0032
S ~ 1.0178
5E10 - SCLC
@ 350K Positive Cycle
S ~ 1.0004
S ~ 1.0745
S ~ 1.0084
5E10 - SCLC
@ 300K Positive Cycle
S ~ 1.0046
S ~ 1.2659
S ~ 1.0151
5E10 - SCLC
@ 350 K Negative Cycle
S ~ 1.0101
S ~1.2158
S ~ 1.01352
5E10 - SCLC
@ 300K Negative Cycle
S ~ 1.4106
S ~ 1.8455
S ~ 2.1129
S ~ 1.1719
S ~ 2.4093
S ~ 1.8069
5E10 - SCLC
@ 100K Positive Cycle
S ~ 1.3919
S ~ 2.5992
S ~ 1.1224
S ~ 1.8895
S ~ 1.8316
S ~ 1.1422
5E10 - SCLC
@ 100K Negative Cycle
(c)
S ~ 0.9716
5E11 - SCLC
@ 350K positive Cycle
S ~ 0.9615
5E11 - SCLC
@ 300K Positive Cycle
S ~ 0.9765
5E11 - SCLC
@ 350K Negative Cycle
S ~ 0.9764
5E11 - SCLC
@ 300K Negative Cycle
S ~ 1.0019
S ~ 1.6347
S ~1.1244
S ~1.2590
5E11 - SCLC
@ 100K Positive Cycle
S ~ 0.7676
S ~ 1.6981
S ~ 0.9694
S ~ 1.2346
5E11 - SCLC
@ 100K Negative Cycle
(d)
S ~ 0.9925
S ~1.0138
5E12 - SCLC
@ 350K Positive Cycle
S ~ 1.0102
S ~ 1.0624
S ~ 1.0037
5E12 - SCLC
@ 300K Positive Cycle
S ~ 0.9968
S ~1.0649
5E12 - SCLC
@ 350K Negative Cycle
S ~ 1.0135
S ~1.1371
S ~ 1.0172
5E12 - SCLC
@ 300K Negative Cycle
S ~ 1.2675
S ~ 1.2246
S ~ 1.4035
5E12 - SCLC
@ 100K Positive Cycle
S ~1.1367
S ~ 1.0892
S ~1.5054
S ~ 1.3159
5E12 - SCLC
@ 100K Negative Cycle
log J (A/cm²)
log E (V/cm²)

◂**Fig. 6** SCLC fitting of positive and negative cycles of I–V data taken at 100 K, 300 K, and 350 K for (a) pristine and (b) 5E10-, (c) 5E11-, and (d) 5E12-fluence irradiated BCFO / LNO /LAO heterostructures.

linear track-like features with hillocks/humps near the track results in similar but lower RS as compared to the 5E10-irradiated heterostructure. In addition, the absence of RS at 100 K is due to the increased structural defects, which can trap the charge carriers and hence requires much higher voltages to release them.

To qualitatively understand the charge conduction mechanism in the pristine and irradiated BCFO/LNO/LAO heterostructures, various charge conduction mechanisms are applied to the cyclic I–V curves. The general conduction mechanisms for ferroelectric thin films are (i) space-charge-limited conduction (SCLC), (ii) Schottky emission or thermionic emission, (iii) Fowler–Nordheim (F–N) tunneling, and (iv) Poole–Frenkel (P–F) emission. Figure 6a, b, c, and d show the fitted cyclic I–V curves of the pristine and irradiated BCFO/LNO/LAO heterostructures using the SCLC mechanism. The SCLC mechanism can be described by Eq 2, as follows:

$$J = \frac{9}{8}\varepsilon_r\varepsilon_0\theta\mu\frac{E^2}{d^3} \tag{2}$$

where μ is electron mobility, ε_r is the optical dielectric constant, ε_0 is the permittivity of free space, E is the applied electric field, d is the film thickness, and θ is the ratio of the free to trapped carrier concentration. Linear fitting of log J versus log E for the BCFO/LNO/LAO heterostructure is shown in the graph in Fig. 6.

Linear fitting in the low-resistance state (LRS) with a slope of ~1 demonstrates that linear ohmic behavior governs the conduction in Ca-doped BFO/LNO/LAO films, whereas in the high-resistance state (HRS), trap-controlled SCLC explains the conduction.[20] In the present case, the slope of I–V data for the pristine heterostructure shows values of ~1.0 for all temperatures, indicating ohmic behavior, while for the 5E10-irradiated heterostructure, slope values are between ~1.0 and 2.5. suggesting dominance of the SCLC mechanism. In addition, the values for 100 K, 5E10-irradiated heterostructure are ~1.8–2.5, confirming the detrapping of charge carriers and validating the SCLC mechanism. Again, ohmic behavior is observed in 5E11-irradiated heterostructures for 300 K and 350 K, while for 100 K, the slope for the HRS increases from ~1.2 to 1.6, indicating the SCLC mechanism. Similarly, with 5E11-fluence irradiation, the calculated slope values for the HRS are from ~1.2 to 1.6 for 5E12-irradiated data at 100 K. Finally, the RS behavior of the BCFO/LNO/LAO heterostructures is attributed to the defect-induced trap charges released under the applied electric field, which can be qualitatively explained by the temperature-dependent behavior. At 100 K, defect-induced trap charges migrate under the applied electric field and create the HRS state in cycle 1, and the already formed conduction path facilitates the movement of charge carriers; thus the LRS in cycle 2 similarly occurs in negative bias. The F–N tunneling, P–F emission, and Schottky emission do not fit well for the proposed devices and hence are not presented here.

Conclusions

The effects of 80 MeV O^{7+} ion irradiation on the properties of PLD-grown BCFO/LNO/LAO heterostructures have been investigated with respect to OVs, structural defects, and interface modification. XRD measurements confirm the single-phasic nature along with the strain modulation with ion irradiation. The strain value decreases for 5E10 ion fluence due to the internal annealing effect, and for 5E11 and 5E12 ion fluence, the strain value increases due to the formation of structural defects, which can be correlated with the decrease in the RMS roughness and the granular structure of 5E10 fluence, which increases for 5E11- and 5E12-ion fluence-irradiated heterostructures as shown in AFM analysis. The AFM micrograph reveals the formation of linear track-like features and tracks with hillock-like surface defects for 5E11 and 5E12 fluence irradiation, respectively. The RUMP-simulated RBS data confirm the ~250 nm and ~145 nm thickness of BCFO and LNO layers along with irradiation-induced BCFO/LNO interface mixed phase. A large variation in the BCFO/LNO mixed phase is observed for 5E10 ion fluence irradiation compared with the pristine and 5E11 fluence-irradiated heterostructures. The irradiation-induced modification of temperature-dependent RS behavior is understood by the formation of OVs, structural defects, and interface modifications. The good RS behavior at 300 K and 100 K for 5E10- and 5E12-irradiated heterostructures may be responsible of the formation of OVs, which releases charge carriers under an applied electric field, while the 5E11 heterostructure does not show RS behavior due to the formation of structural defects which hinder the conduction of charge carriers at low voltages. This bipolar RS behavior is also verified by the conduction mechanism, and it is understood that the ohmic and SCLC conduction mechanism plays an important role in the irradiated BCFO/LNO/LAO heterostructures. The ion fluence-dependent modification of the structural strain RMS surface roughness with RS behavior in the BCFO/LNO/LAO heterostructure is summarized in the graphical abstract. Lastly, defects formed by ion irradiation are permanent defects and hence ensure long-term stability of normal devices under ambient conditions.

Acknowledgments The authors are thankful to Dr. Mukul Gupta, UGC-DAE, CSR, Indore, for XRD measurement and Dr. D. S. Rana, IISER, Bhopal, for the PLD facility. The authors also acknowledge Dr. C. Balasubramanian, FCIPT, IPR, Gandhinagar, for providing the AFM facility. ABR is thankful to IUAC New Delhi for UFR-65319 and UFR-72317, and UGC-DAE, CSR, Indore, for CSR-IC-ISUM-64/CRS-347/2020-21/949 and project funding. S.H. acknowledges the DST-INSPIRE for Fellowship (DST/INSPIRE/03/2023/000106). J. S. acknowledges the DST-INSPIRE for Fellowship (DST/INSPIRE/03/2018/000699).

Conflict of interest On behalf of all authors, the corresponding author states that there is no conflict of interest.

References

1. H. Akinaga, Recent advances and future prospects in functional-oxide nanoelectronics: the emerging materials and novel functionalities that are accelerating semiconductor device research and development. *Jpn. J. Appl. Phys.* 52(10R), 100001 (2013).
2. L. Yin and W. Mi, Progress in $BiFeO_3$-based heterostructures: materials, properties and applications. *Nanoscale* 12(2), 477–523 (2020). https://doi.org/10.1039/c9nr08800h.
3. P. Zubko, S. Gariglio, M. Gabay, P. Ghosez, and J.-M. Triscone, Interface physics in complex oxide heterostructures. *Ann. Rev. Condens. Matter Phys.* 2(1), 141–165 (2011). https://doi.org/10.1146/annurev-conmatphys-062910-140445.
4. G. Catalan and J.F. Scott, Physics and applications of bismuth ferrite. *Adv. Mater.* 21(24), 2463–2485 (2009). https://doi.org/10.1002/adma.200802849.
5. T. Zhao, A. Scholl, F. Zavaliche, K. Lee, M. Barry, A. Doran, M.P. Cruz, Y.H. Chu, C. Ederer, N.A. Spaldin, R.R. Das, D.M. Kim, S.H. Baek, C.B. Eom, and R. Ramesh, Electrical control of antiferromagnetic domains in multiferroic $BiFeO_3$ films at room temperature. *Nat. Mater.* 5(10), 823–829 (2006). https://doi.org/10.1038/nmat1731.
6. D. Lebeugle, D. Colson, A. Forget, M. Viret, A.M. Bataille, and A. Gukasov, Electric-field-induced spin flop in $BiFeO_3$ single crystals at room temperature. *Phys. Rev. Lett.* 100, 227602 (2008). https://doi.org/10.1103/PhysRevLett.100.227602.
7. J. Wang, J.B. Neaton, H. Zheng, V. Nagarajan, S.B. Ogale, B. Liu, D. Viehland, D.G. Schlom, U.V. Waghmare, N.A. Spaldin, K.M. Rabe, M. Wuttig, and R. Ramesh, Epitaxial BiFeO3 multiferroic thin film heterostructures. *Science* 299(5613), 1719–1722 (2003). https://doi.org/10.1002/chin.200324015.
8. P.P. Biswas, Ch. Thirmal, S. Pal, and P. Murugavel, Dipole pinning effect on photovoltaic characteristics of ferroelectric $BiFeO_3$ films. *J. Appl. Phys.* 123(2), 024101 (2018). https://doi.org/10.1063/1.5006311.
9. M. Bibes and A. Barthélémy, Towards a magnetoelectric memory. *Nat. Mater.* 7(6), 425–426 (2008). https://doi.org/10.1038/nmat2189.
10. J. Wu, Z. Fan, D. Xiao, J. Zhu, and J. Wang, Multiferroic bismuth ferrite-based materials for multifunctional applications: ceramic bulks, thin films and nanostructures. *Prog. Mater. Sci.* 84, 335–402 (2016). https://doi.org/10.1016/j.pmatsci.2016.09.001.
11. J. Silva, A. Reyes, H. Esparza, H. Camacho, and L. Fuentes, $BiFeO_3$: a review on synthesis, doping and crystal structure. *Integr. Ferroelectr.* 126(1), 47–59 (2011). https://doi.org/10.1080/10584587.2011.574986.
12. R. Safi and H. Shokrollahi, Physics, chemistry and synthesis methods of nanostructured bismuth ferrite ($BiFeO_3$) as a ferroelectric-magnetic material. *Progr. Solid State Chem.* 40(1–2), 6–15 (2012).
13. F. Fan, M. Duan, B. Luo, and C. Chen, Ferroelectric, magnetoelectric and photoelectric properties of $BiFeO_3$ /$LaNiO_3$ heterostructure. *Chin. J. Phys.* 56(5), 1903–1908 (2018). https://doi.org/10.1016/j.cjph.2018.08.002.
14. V. Pyragas, V. Lisauskas, K. Šliužienė, and B. Vengalis, Electrical properties of nonstoichiometric In_2O_{3-x}thin films. *Lith. J. Phys.* 51(1), 47–51 (2011). https://doi.org/10.3952/lithjphys.51109.
15. K.P. Rajeev, G.V. Shivashankar, and A.K. Raychaudhuri, Low-temperature electronic properties of a normal conducting perovskite oxide ($LaNiO_3$). *Solid State Commun.* 79(7), 591–595 (1991). https://doi.org/10.1016/0038-1098(91)90915-i.
16. N.C. Pandya, A.K. Debnath, and U.S. Joshi, Resistance switching and memory effects in solution-processed $BiFeO_3$/$LaNiO_3$ junctions. *J. Phys. D Appl. Phys.* 49(5), 055301 (2015). https://doi.org/10.1088/0022-3727/49/5/055301.
17. S. Hussain, S.K. Hasanain, G. Hassnain Jaffari, and S. Ismat Shah, Thickness dependent magnetic and ferroelectric properties of $LaNiO_3$ buffered $BiFeO_3$ thin films. *Curr. Appl. Phys.* 15(3), 194–200 (2015).
18. Z. Zhang, P. Wu, L. Chen, and J. Wang, First-principles prediction of a two dimensional electron gas at the $BiFeO_3$/$SrTiO_3$ interface. *Appl. Phys. Lett.* 99(6), 062902 (2011). https://doi.org/10.1063/1.3624457.
19. G. Chen, J. Chen, W. Pei, Y. Lu, Q. Zhang, Q. Zhang, and Y. He, Bismuth ferrite materials for solar cells: current status and prospects. *Mater. Res. Bull.* 110, 39–49 (2019). https://doi.org/10.1016/j.materresbull.2018.10.011.
20. S. Jethva, S. Katba, M. Bhatnagar, M. Ranjan, D. Shukla, and D.G. Kuberkar, Effect of strain on the modifications in electronic structure and resistive switching in Ca-doped $BiFeO_3$ films. *J. Appl. Phys.* 125(8), 082510 (2019). https://doi.org/10.1063/1.5045844.
21. Y.-T. Liu, S.-J. Chiu, H.-Y. Lee, and S.-Y. Chen, Preparation of a $BiFeO_3$/$LaNiO_3$ multiferroic oxide superlattice structure by RF magnetron sputtering. *Surf. Coat. Technol.* 206(7), 1666–1672 (2011). https://doi.org/10.1016/j.surfcoat.2011.08.030.
22. A.B. Ravalia, M.V. Vagadia, P.G. Trivedi, P.S. Solanki, P.S. Vachhani, R.J. Choudhary, D.M. Phase, K. Asokan, N.A. Shah, and D.G. Kuberkar, Modifications in device characteristics of La06Pr02Sr02MnO3/SrNb0002Ti0998O3 manganites by swift heavy ion irradiation. *Indian J. Phys.* 89(2), 137–142 (2014).
23. M. Bianconi, N. Argiolas, M. Bazzan, G.G. Bentini, M. Chiarini, A. Cerutti, P. Mazzoldi, G. Pennestrì, and C. Sada, On the dynamics of the damage growth in 5 MeV oxygen-implanted lithium niobate. *Appl. Phys. Lett.* 87(7), 072901 (2005). https://doi.org/10.1063/1.2007855.
24. J.H. Markna, R.N. Parmar, D.G. Kuberkar, R. Kumar, D.S. Rana, and S.K. Malik, Thickness dependent swift heavy ion irradiation effects on electronic transport of $(La_{0.5}Pr_{0.2})Ba_{0.3}$MnO3 thin films. *Appl. Phys. Lett.* 88(15), 152503 (2006). https://doi.org/10.1063/1.2192087.
25. D. Avasthi, Role of swift heavy ions in materials characterization and modification. *Vacuum* 48(12), 1011–1015 (1997). https://doi.org/10.1016/s0042-207x(97)00114-0.
26. S.B. Ogale, Y.H. Li, M. Rajeswari, L.S. Riba, R. Ramesh, T. Venkatesan, A.J. Millis, R. Kumar, G.K. Mehta, R. Bathe, and S.I. Patil, Columnar defect induced phase transformation in epitaxial $La_{0.7}Ca_{0.3}$MnO3 films. *J. Appl. Phys.* 87(9), 4210–4215 (2000).
27. Ch. Houpert, F. Studer, D. Groult, and M. Toulemonde, Transition from localized defects to continuous latent tracks in magnetic insulators irradiated by high energy heavy ions: A HREM investigation. *Nucl. Instrum. Methods Phys. Res., Sect. B* 39(1–4), 720–723 (1989). https://doi.org/10.1016/0168-583x(89)90882-3.
28. H. Yamamura and R. Kiriyama, (1972) The relations between oxygen vacancies and structures in the solid solution systems

$Sr_{1-x}M_xFeO_{3-\delta}$ (M=Y, La, Bi and ln), 2, 343–349 https://doi.org/10.1246/nikkashi.1972.343
29. W. Jo, D.C. Kim, and J.W. Hong, Reverse-poling effects on charge retention in Pb(Zr, Ti)$_O$3(001)/LaNi$_O$3(001) heterostructures. *Appl. Phys. Lett.* 76(3), 390–392 (2000). https://doi.org/10.1063/1.125763.
30. M. Detalle and D. Rémiens, Chemical and physical characterization of $LaNiO_3$ thin films deposited by sputtering for top and bottom electrodes in ferroelectric structure. *J. Cryst. Growth* 310(15), 3596–3603 (2008). https://doi.org/10.1016/j.jcrysgro.2008.04.053.
31. J. Wu and J. Wang, Ferroelectric and impedance behavior of La- and Ti-Co doped $BiFeO_3$ thin films. *J. Am. Ceram. Soc.* 93(9), 2795–2803 (2010). https://doi.org/10.1111/j.1551-2916.2010.03816.x.
32. J.F. Ziegler, J. P. Biersack, and M. D. Ziegler, see http://www.srim.org.for Program SRIM, 2008
33. A. Ravalia, M. Vagadia, P.S. Solanki, K. Asokan, and D.G. Kuberkar, Role of strain and nanoscale defects in modifying the multiferroicity in nanostructured $BiFeO_3$ films. *J. Exp. Nanosci.* 10(14), 1057–1067 (2014). https://doi.org/10.1080/17458080.2014.953608.
34. D.K. Shukla, S. Ravi Kumar, R.J. Mollah, P. Choudhary, S.K. Thakur, N.B. Sharma, and M.K. Brookes, Swift heavy ion irradiation induced magnetism in magnetically frustrated $BiMn_2O_5$ thin films. *Phys. Rev. B* 82(17), 174432 (2010). https://doi.org/10.1103/physrevb.82.174432.
35. A. Ravalia, M. Vagadia, P.S. Solanki, S. Gautam, K.H. Chae, K. Asokan, N.A. Shah, and D.G. Kuberkar, Role of defects in $BiFeO_3$ multiferroic films and their local electronic structure by x-ray absorption spectroscopy. *J. Appl. Phys.* 116(15), 153701 (2014). https://doi.org/10.1063/1.4898196.
36. Z.-X. Lu, X. Song, L.-N. Zhao, Z.-W. Li, Y.-B. Lin, M. Zeng, Z. Zhang, X.-B. Lu, S.-J. Wu, X.-S. Gao, Z.-B. Yan, and J.-M. Liu, Temperature dependences of ferroelectricity and resistive switching behavior of epitaxial $BiFeO_3$ thin films. *Chin. Phys. B* 24(10), 107705 (2015). https://doi.org/10.1088/1674-1056/24/10/107705.
37. Y. Watanabe and M. Okano, Photoresponse of Zener tunneling junctions of Pb(Ti, Zr)$_O$3/SrTi$_O$3 at low temperature. *J. Appl. Phys.* 94(11), 7187–7192 (2003). https://doi.org/10.1063/1.1625085.